DEVELOPMENT AND VALIDATION OF A SURFACE TENSION MODEL FOR THE MESHLESS-FINITE-MASS METHOD

M. Wicker*, M. Okraschevski*, R. Koch*, H.-J. Bauer*
* Karlsruhe Institute of Technology, Institute of Thermal Turbomachinery, Straße am Forum 6, Karlsruhe, Germany

Abstract

In an effort to improve the accuracy of numerical investigations of air-blast atomization in jet engines, the potential of the new Meshless-Finite-Mass method (MFM) is being investigated. Since this method is not yet equipped to handle engineering applications, MFM is extended to include surface tension effects. The surface tension model is validated against droplet oscillation benchmarks. Subsequently, this novel method is compared to an established method, the Smoothed Particle Hydrodynamics in a new, simplified primary atomization benchmark case, where a significant improvement is observed.

Keywords

Primary atomization; Computational Fluid Dynamics; Surface tension

NOMENCLATURE

Symbols

$\vec{A}$	effective face area	m^2
a	numerical speed of sound	m/s
$\tilde{c}$	inter-particle density averaged color	
c	color function	
d	number of dimensions	kg
	total specific energy	J/kg
$\boldsymbol{E}$	matrix for the moving least squares gradient estimator	
$\boldsymbol{F}$	flux tensor	
$\vec{f}$	acceleration vector	m/s
f	arbitrary scalar field	
γ	polytropic exponent	
h	smoothing length	m
$\boldsymbol{I}$	identity tensor	
κ	curvature	1/m
m	mass	kg
$\vec{n}$	interface normal vector	m
ω	kernel normalization term	
p	pressure	N/m^2
ψ	volume fraction	
ρ	density	kg/m^3
σ	surface tension	N/m
t	physical time	
$\boldsymbol{\tau}$	shear stress tensor	
$\vec{U}$	state vector	
$\vec{u}$	velocity	m/s
V	volume	m^3
W	kernel function	
$\vec{x}$	coordinates	m

Indices

0	reference value
i	associated with particle i
j	associated with particle j
surf	surface tension
visc	viscous

Abbreviations

CFD	Computational Fluid Dynamics
CSF	Continuum Surface Force
MFM	Meshless Finite Mass
MLS	Moving Least Squares
SPH	Smoothed Particle Hydrodynamics

doi: 10.25967/610505

1. INTRODUCTION

It is to be expected that for the foreseeable future the majority of jet engines will continue to be operated using liquid fuel in the form of either kerosene or sustainable aviation fuels. Therefore, liquid fuel atomization is a key process in the continuing research effort aiming to lower the emissions of pollutants like NOx and soot. The fuel atomization process in jet engines is realized through air-blast atomizers in which a thin film of fuel is disintegrated through the shear stress imposed by the surrounding air flow. This process can be divided into primary atomization and secondary atomization domains, the former being the focus of the present study. In the primary atomization domain close to the atomization edge the flow is not only characterized by high pressures and temperatures but also by a very dense spray consisting of non-spherical liquid fragments. These conditions make experimental investigation highly expensive and complex, if not impossible. Consequently, numerical analysis is the method of choice.

However, the numerical investigation of primary atomization is also uniquely challenging, most importantly due to the extremely broad range of length scales with the domain size determined by the nozzle geometry in the order of centimeters and the smallest resulting droplets in the order of a few micrometers. Furthermore, the disintegration of the liquid film entails extreme deformation of the interface between liquid and gaseous phase, posing numerical challenges for the employed methods. Consequently, while mesh-based Eulerian approaches are predominantly used in most technical applications of computational fluid dynamics (CFD), particle-based Lagrangian methods offer some advantages regarding the investigation of primary atomization. The phase interfaces and its deformation are inherently captured due to the Lagrangian nature as the particles are advected with the flow. Furthermore, these methods exhibit a superior performance in highly parallelized simulations, facilitating the utilization of a higher number of cores, thereby reducing the wall-clock time of massive high-fidelity simulations [1].

Smoothed Particle Hydrodynamics (SPH) is an established tool in this realm and has been numerously employed [1–4]. This method was originally developed for astrophysical applications [5, 6] but has long been employed in an engineering context [7]. However, in comparison to mesh-based methods, SPH is less mature and therefore requires further research efforts for further method development. Crucial to the investigation of air-blast atomization, SPH exhibits excessive numerical dissipation in turbulent flows [8].

Similar to the emergence of SPH, a new Lagrangian methods has been gaining popularity in the astrophysics community, the Meshless-Finite-Mass method (MFM) [9]. This new method can be classified as a Lagrangian Finite-Volume method and promises to improve on SPH, critically alleviating the excessive numerical dissipation in turbulent applications. As the use of MFM so far has been limited to the astrophysics community, the method lacks some necessary features for engineering applications. Most crucial is the addition of a surface tension model in order to facilitate multi-phase simulations. By virtue of the similarity between SPH and MFM though, models developed for the former can be transferred to the latter. Therefore, as a first step, the commonly used SPH surface tension model developed by Adami et al. [10] is implemented into the open source MFM code *GIZMO* [9]. Additionally, a new MFM-native surface tension formulation is developed. Both formulations are evaluated through an oscillating droplet benchmark.

The validation of an MFM implementation incorporating surface tension effects enables for the first time a comparison with SPH in industrially relevant multi-phase flow applications. The enormous computational cost as well as the lack of other necessary features such as appropriate boundary conditions preclude a comparison of complete, high-fidelity primary atomization simulations [1–4]. Therefore, an analogon is needed. The Kelvin-Helmholtz instability is an ideal candidate for this, as it is one of the primary instabilities in air-blast atomization, as well as a commonly used benchmark case [9, 11–13]. In order to comply with the limitations of the present MFM code, a numerical setup similar to the one described by Lecoanet et al. [11] is combined with a physical configuration akin to the liquid atomization as described by Chaussonnet et al. [3]. As a reference point, the MFM simulations are compared to results obtained with *turboSPH*, the same SPH code that was used for previous primary atomization simulations [1–4] and was specifically designed for application in this field. A comparison of the resulting flow fields and discussion of the influence of spatial resolution finally enables an early but qualified analysis of the potential of MFM in a primary atomization context.

2. NUMERICAL METHODS

In this section the fundamental principles behind the employed numerical methods will be outlined. A more rigorous derivation can be found in the appropriate literature, e.g. [14] and [9] for SPH and MFM, respectively.

2.1. Smoothed Particle Hydrodynamics

In SPH, each particle i is associated with a finite fraction of the fluid with a constant mass m_i and is advected with the fluid velocity u_i. Using a smoothing kernel W, the value f_i of an arbitrary scalar field $f(\vec{x})$ at the position $\vec{x}_\mathrm{i}$ of particle i can be approximated through weighted summation over its neighbors j as

$$\langle f \rangle_\mathrm{i} = \langle f(\vec{x}_\mathrm{i}) \rangle = \sum_j f(\vec{x}_\mathrm{j}) V_\mathrm{j} W(\vec{x}_\mathrm{i} - \vec{x}_\mathrm{j}, h) \; . \tag{1}$$

The gradient of f can be approximated accordingly using the kernel gradient $\vec{\nabla}W$, which can be derived analytically:

$$\langle \vec{\nabla} f \rangle_{\mathrm{i}} = \sum_j f(\vec{x}_{\mathrm{j}}) V_{\mathrm{j}} \vec{\nabla} W(\vec{x}_{\mathrm{i}} - \vec{x}_{\mathrm{j}}, h) \ . \tag{2}$$

In Equations (1) and (2), h denotes the smoothing length, the characteristic length scale of the smoothing kernel. The particle volume V_{i} is computed from the constant particle mass m_{i} and the density ρ_{i}. The density is approximated using the multi-phase formulation by [15]:

$$\langle \rho \rangle_{\mathrm{i}} = m_{\mathrm{i}} \sum_j V_{\mathrm{j}} W(\vec{x}_{\mathrm{i}} - \vec{x}_{\mathrm{j}}, h) \ . \tag{3}$$

The momentum equation is formulated as

$$\langle \frac{d\vec{u}}{dt} \rangle_{\mathrm{i}} = \sum_j \frac{(p_{\mathrm{i}} + p_{\mathrm{j}})}{\rho_{\mathrm{i}} \rho_{\mathrm{j}}} m_{\mathrm{j}} \vec{\nabla} W(\vec{x}_{\mathrm{i}} - \vec{x}_{\mathrm{j}}, h) + \vec{f}_{\mathrm{visc,i}} + \vec{f}_{\mathrm{surf,i}} \ . \tag{4}$$

The viscous term is modelled using the approach by Szewc [16] and surface tension forces are discussed in depth in section 3. In order to close the set of equations, the pressure p is linked to the density ρ through the barotropic, weakly-compressible equation of state [17]:

$$p - p_0 = \frac{\rho_0 a^2}{\gamma} \left[\left(\frac{\rho}{\rho_0} \right)^{\gamma} - 1 \right] \ , \tag{5}$$

Here, a is numerical speed of sound, γ the polytropic exponent and the index 0 denotes the reference values of pressure and density.

2.2. Meshless-Finite-Mass

MFM is a Lagrangian member of a class of Arbitrary Langrangian-Eulerian (ALE) mesh-free methods developed by Hopkins [9, 18], based on the work of Lanson and Vila [19, 20]. It is implemented in the open source code *GIZMO*, which is a highly modified version of *Gadget* [21]. It can be derived from the set of transport equations for mass, momentum and energy in an ALE frame of reference:

$$\frac{\partial \vec{U}}{\partial t} + \vec{\nabla} \cdot (\boldsymbol{F} - \vec{u}_{\mathrm{frame}} \otimes \vec{U}) = \vec{0} \ , \tag{6}$$

wherein $\vec{u}_{\mathrm{frame}}$ is the frame velocity of the individual particles. The state vector $\vec{U}$ and the flux tensor $\boldsymbol{F}$ are given by

$$\vec{U} = \begin{pmatrix} \rho \\ \rho \vec{u} \\ \rho e \end{pmatrix} \ , \tag{7}$$

$$\boldsymbol{F} = \begin{pmatrix} \rho \vec{u} \\ \rho \vec{u} \otimes \vec{u} + p \boldsymbol{I} - \boldsymbol{\tau} \\ (\rho e + p) \vec{u} \end{pmatrix} \ . \tag{8}$$

Here, $\vec{u}$ denotes the velocity, e the total specific energy, p the pressure, $\boldsymbol{\tau}$ the shear stress tensor and $\boldsymbol{I}$ the identity tensor. Note that the energy equation is not solved in this study as only isothermal flows are considered. As MFM is a Lagrangian method, the frame velocity $\vec{u}_{\mathrm{frame}}$ is set to the fluid velocity $\vec{u}$.
Like in SPH, the kernel function W with its smoothing length h is used to discretize the domain. For every point $\vec{x}$ a volume fraction Ψ_{i} associated with a particle i is determined by

$$\psi_{\mathrm{i}}(\vec{x}) = \frac{1}{\omega(\vec{x})} W(\vec{x} - \vec{x}_{\mathrm{i}}, h) \ , \tag{9}$$

$$\omega(\vec{x}) = \sum_j W(\vec{x} - \vec{x}_{\mathrm{j}}, h) \ . \tag{10}$$

The 'effective' volume of a particle i is then

$$V_{\mathrm{i}} = \int \psi_{\mathrm{i}}(\vec{x}) d\vec{x} \ . \tag{11}$$

However, unlike in SPH, gradients are not approximated using the kernel gradient, but rather through a second-order accurate, locally centered least-squares matrix gradient estimator. In combination, this is used to rewrite (6) in a Galerkin-type approach as

$$\frac{d}{dt}(V_{\mathrm{i}} \vec{U}_{\mathrm{i}}) + \sum_j \tilde{\boldsymbol{F}}_{\mathrm{ij}} \cdot \vec{A}_{\mathrm{ij}} = \vec{0} \ . \tag{12}$$

It is important to note that A_{ij} is not a geometric face area but rather an 'effective face area' that is moving with a frame velocity such that mass is conserved on both sides of the face. The flux $\tilde{\boldsymbol{F}}_{\mathrm{ij}}$ at the interface is the solution of a Riemann problem between particles i and j. This Riemann problem is solved employing an HLLC Riemann solver [22].

3. SURFACE TENSION MODEL

Most surface tension models for SPH can be grouped into one of two categories: Pseudo-molecular models [23] or Continuum Surface Force (CSF) models [24]. In the context of primary atomization, CSF models, specifically the formulation by Adami et al. [10] have proven to be more reliable in handling the high interface density ratios and deformation.
In a CSF model, the distinct phases are distinguished through the color function c. The discontinuous surface tension force is replaced by a continuous force acting on all particles in the vicinity of the interface, i.e. all particle for which the norm of the gradient of the color function $\|\vec{\nabla} c\|$ is non-zero. The surface tension term in (4) in the case of a constant surface tension σ

is consequently expressed as

$$\vec{f}_{\mathrm{surf,i}} = \frac{1}{\rho_i}\sigma\kappa_\mathrm{i}\vec{\nabla}c_\mathrm{i} \ . \tag{13}$$

Mathematically, the curvature κ is defined with the divergence of the interface normal vector $\vec{n}$ as

$$\kappa = -\left(\vec{\nabla}\cdot\vec{n}\right) \ , \tag{14}$$

and in turn, the normal vector is given by

$$\vec{n} = \frac{\vec{\nabla}c}{\|\vec{\nabla}c\|} \tag{15}$$

The formulation by Adami et al. [10] and the new formulation that will be outlined in the following differ in the manner in which the color gradient and curvature are computed.

3.1. Kernel gradient formulation

In the SPH-type surface tension formulation by Adami et al. [10] the color function is defined for each combination of particles k and l as

$$c_l^k = \begin{cases} 1, & \text{if particles } k \text{ and } l \text{ are not of the same phase,} \\ 0, & \text{if particles } k \text{ and } l \text{ are of the same phase.} \end{cases} \tag{16}$$

In order to handle high interface ratios, the color is substituted by the inter-particle density averaged color value, thereby ensuring matching accelerations of particles with high mass disparity:

$$\tilde{c}_\mathrm{ij} = \frac{\rho_\mathrm{j}}{\rho_\mathrm{i}+\rho_\mathrm{j}}c_\mathrm{i}^\mathrm{i} + \frac{\rho_\mathrm{i}}{\rho_\mathrm{i}+\rho_\mathrm{j}}c_\mathrm{j}^\mathrm{i} \ . \tag{17}$$

Using the shortened notation for the kernel gradient $\vec{\nabla}W_\mathrm{ij} = \vec{\nabla}W(\vec{x}_\mathrm{i}-\vec{x}_\mathrm{j},h)$, the color gradient is computed through

$$\vec{\nabla}c_\mathrm{i} = \frac{1}{V_\mathrm{i}}\sum_j [V_\mathrm{i}^2 + V_\mathrm{j}^2]\tilde{c}_\mathrm{ij}\vec{\nabla}W_\mathrm{ij} \ . \tag{18}$$

Combining (15), (18) and the number of dimensions d a reproducing divergence approximation for the curvature κ is derived:

$$\kappa_\mathrm{i} = -d\frac{\sum_j(\vec{\hat{n}}_\mathrm{i}-\vec{\hat{n}}_\mathrm{j})\cdot\vec{\nabla}W_\mathrm{ij}V_\mathrm{j}}{\sum_j\|\vec{\nabla}W_\mathrm{ij}\|V_\mathrm{j}} \ . \tag{19}$$

3.2. Moving least squares formulation

In contrast to SPH, where gradients are evaluated using the kernel gradient, MFM employs a moving least squares (MLS) gradient estimator. As the key elements in the SPH surface tension model are the computation of the color gradient and divergence of the normal vector, it appears logical to apply the same gradient estimator to these terms. Consequently, in this new surface tension formulation the color gradient is given by

$$\nabla c_i = \boldsymbol{E}_i^{-1}\sum_j 2\ \tilde{c}_\mathrm{ij}\psi_\mathrm{j}(\vec{x}_\mathrm{i})\left(\vec{x}_\mathrm{j}-\vec{x}_\mathrm{i}\right) \ , \tag{20}$$

with the components $E_\mathrm{i}^{\alpha\beta}$of the matrix $\boldsymbol{E}_i$:

$$E_\mathrm{i}^{\alpha\beta} = \sum_j \left(\vec{x}_\mathrm{j}-\vec{x}_\mathrm{i}\right)^\alpha\left(\vec{x}_\mathrm{j}-\vec{x}_\mathrm{i}\right)^\beta\psi_\mathrm{j}(\vec{x}_\mathrm{i}) \ . \tag{21}$$

The Jacobian matrix of the normal vector is computed likewise:

$$\nabla\otimes\vec{\hat{n}} = \left(\nabla\hat{n}^\mathsf{x} \quad \nabla\hat{n}^\mathsf{y} \quad \nabla\hat{n}^\mathsf{z}\right)^\mathsf{T} \ , \tag{22}$$

$$\nabla\hat{n}^\alpha = \boldsymbol{E}_\mathrm{i}^{-1}\sum_j\left(\hat{n}_\mathrm{j}^\alpha-\hat{n}_\mathrm{i}^\alpha\right)\psi_\mathrm{j}(\vec{x}_\mathrm{i})\left(\vec{x}_\mathrm{j}-\vec{x}_\mathrm{i}\right) \ . \tag{23}$$

With (14), the curvature is evaluated for each particle through the trace of the Jacobian.

4. VALIDATION OF THE SURFACE TENSION MODEL

4.1. Implementation of the SPH formulation in MFM

The kernel gradient surface tension model is validated against a subset of the droplet benchmark from the original publication by Adami et al. [10]. First, the deformation of an initially square droplet with the edge length $l_\mathrm{d} = 0.6$ in a square domain with the edge length $L = 2$ under surface tension $\sigma = 1$ is predicted. The density of both fluids is set to $\rho_0 = 1$ with a dynamic viscosity $\mu = 0.05$. All variables are denoted in code units as the scale is arbitrary. The domain is discretized using 3600 particles and a Wendland C4 kernel [25] with 32 neighbors, approximately equivalent to a ratio of smoothing length to particle spacing of $h/dx = 1.5$ [26]. The artificial speed of sound, background pressure and polytropic ratio are set to $a = 20$, $p_0 = 100$ and $\gamma = 1$, respectively. The particle arrangement and droplet shape are depicted in Fig. 1 for the initial state and once the equilibrium state is reached at $t_\mathrm{eq} = 0.4$. Evidently, the model correctly predicts the circular equilibrium shape while maintaining a good particle order.
In the second validation case, a circular droplet with a radius $r_d = 0.2$ is placed in a square domain with the edge length $L = 1$. The domain is discretized using 14400 particles, and again the Wendland C4 kernel with $h/dx = 1.5$ is used. The droplet density and viscosity are once again set to $\rho_\mathrm{d} = 1$ and $\mu_\mathrm{d} = 0.05$, the density and viscosity ratio between the two fluids however are $\Phi = \rho_\mathrm{d}/\rho_\infty = 1000$ and $\lambda = \mu_\mathrm{d}/\mu_\infty = 100$. The background pressure is again set to $p_0 = 100$, and the polytropic ratio of the droplet and surrounding fluid to $\gamma_\mathrm{d} = 7$ and $\gamma_\infty = 1$, respectively. The artificial speeds of sound are $a_\mathrm{d} = 30$ and $a_\infty = 359$, follow-

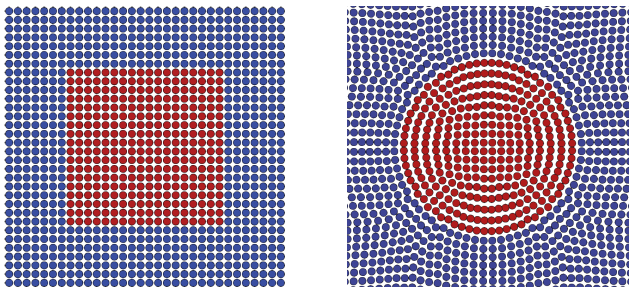

(a) $t = 0$ **(b)** $t = t_{\text{eq}}$

FIG 1. Droplet shape in the square droplet deformation case using the kernel gradient surface tension model.

ing the impedance matching technique as described by Chaussonnet et al. [3]. The oscillation is induced by a prescribed initial droplet velocity field with $U_0 = 1$ and $r_0 = 0.05$:

$$U_{\text{x}} = U_0 \frac{x}{r_0} \left(1 - \frac{y^2}{r_0 r}\right) \exp\left(-\frac{r}{r_0}\right) , \tag{24}$$

$$U_{\text{y}} = -U_0 \frac{y}{r_0} \left(1 - \frac{x^2}{r_0 r}\right) \exp\left(-\frac{r}{r_0}\right) . \tag{25}$$

The relation between surface tension σ and oscillation period T is shown in Figure 2, along with the analytical solution

$$T_{th} = 2\pi \sqrt{\frac{r_d^3 \rho_d}{6\sigma}} . \tag{26}$$

The numerical results show excellent agreement with

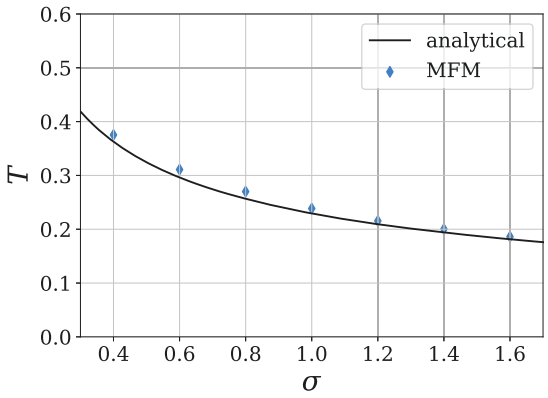

FIG 2. Oscillation period T in the oscillating droplet case using the kernel gradient surface tension model for varied surface tension values σ.

the analytical solution. As result of the validation, it is confirmed that surface tension model, which was originally developed for SPH integrates well into MFM.

4.2. New MLS formulation

To explore the novel surface tension formulation using the MLS gradient estimator, the square droplet deformation case is computed using 14400 particles. In addition to the configuration described in the previous section, a second case is computed with the fluid parameters from the circular droplet oscillation of the previous case and the surface tension $\sigma = 1$. Figure 3 shows snapshots of the particle distributions from both simulations. While the droplet shape appears to

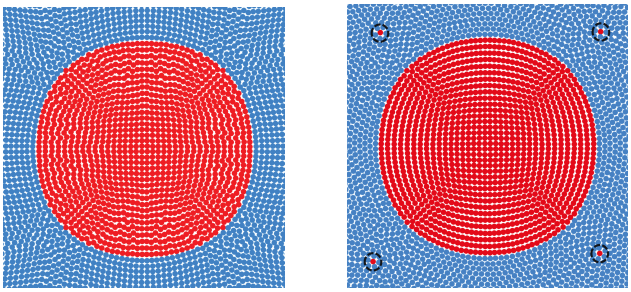

(a) $\Phi = 1,\ t = 0.4$ **(b)** $\Phi = 1000,\ t = 0.1$

FIG 3. Droplet shape in the square droplet deformation case the MLS surface tension model with different density ratios Φ at the physical time t.

be plausible for $\Phi = 1$, the snapshot from the simulation with $\Phi = 1000$ shows that the corner particles indicated by the black circles have been pinched off from the droplet. This reveals a crucial weakness of the MLS approach. Even though the curvature at the discontinuity at the corner of the droplet is theoretically infinite, the numerical solution obtained from the initial particle distribution using the MLS estimator is zero. For the higher density ratio this numerical error is evidently impactful enough to cause the unphysical detachment of the corner particles from the droplet. Here, the smoothing in the kernel gradient model appears to increase the robustness of the surface tension calculation. As robustness is crucial, this approach is used for all further simulations.

5. KELVIN-HELMHOLTZ INSTABILITY BENCHMARK

Upon demonstrating that by integrating the SPH surface tension model into MFM, surface tension effects can be correctly predicted, the next step is a first assessment of the potential improvement that can be gained through the use of MFM in technically relevant multi-phase flows.

Comprehensive primary atomization simulations require an enormous amount of computational resources. Furthermore, suitable boundary conditions are of the utmost importance. As *GIZMO* lacks the latter and the former is impractical for this fundamental comparison, a simplified primary atomization benchmark is proposed. The Kelvin-Helmholtz instability is identified as the ideal candidate for this, as it is both a common benchmark case as well as one of the primary instabilities in air-blast atomization. In the original publication [9], Hopkins was able to show, that MFM was superior in an academic Kelvin-Helmholtz benchmark case [12] compared to two considered

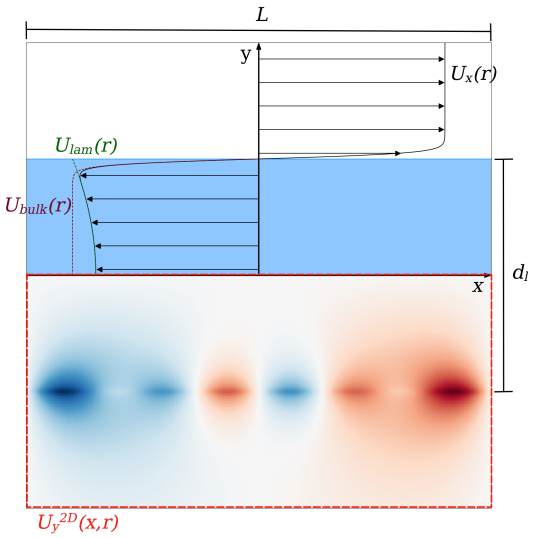

FIG 4. Sketch of the initial velocity distribution U in the 2D Kelvin-Helmholtz instability case.

SPH schemes. Even though SPH can be employed to reproduce converged reference solutions in simplified benchmarks [13], it is uncertain how this will translate to the instabilities occurring during primary atomization. Hence, a modified Kelvin-Helmholtz benchmark is described in the following. This benchmark is subsequently used to evaluate *GIZMO* with the added surface tension model and compare it to the proprietary SPH code *turboSPH* in both two- and three-dimensional simulations.

5.1. Setup

The physical configuration is based on the work by Chaussonnet et al. [3] and the associated reference experiment [27]. The numerical configuration is similar to common benchmarks [11, 12]. A liquid jet with the diameter $d_\mathsf{l} = 2\,\mathrm{mm}$ is placed laterally at the center of a square or respectively cubic domain with the edge length $L = 4\,\mathrm{mm}$. The domain is discretized using N^d particles on a Cartesian lattice and the Wendland C4 kernel with smoothing length h. The fluid properties are given by $\rho_\mathsf{l} = 1233\,\mathrm{kg/m^3}$ and $\mu_\mathsf{l} = 0.2\,\mathrm{Pas}$ for the liquid, $\rho_\mathsf{g} = 13.25\,\mathrm{kg/m^3}$ and $\mu_\mathsf{l} = 18.61\,\mu\mathrm{Pas}$ for the gas, and the surface tension $\sigma = 63.6\,\mathrm{mN/m}$. The parameters in the equation of state for both fluids are $p_0 = 275\,\mathrm{kPa}$, $a_\mathsf{l} = 150\,\mathrm{m/s}$, $\gamma_\mathsf{l} = 7$, $a_\mathsf{g} = 1450.9\,\mathrm{m/s}$ and $\gamma_\mathsf{g} = 1$.
In the reference study [3], the mean gas velocity is $U_\mathsf{g} = 58\,\mathrm{m/s}$ and the velocity of the liquid jet is $U_\mathsf{l} = 0.55\,\mathrm{m/s}$. Here, the initial velocity in main flow direction as sketched in the upper half of Fig. 4 is given by:

(27)
$$U_\mathsf{x}(r) = \begin{cases} U_\mathsf{bulk}(r) + u_\mathsf{lam}(r) & 0 \le r < d_\mathsf{l}/2\,, \\ U_\mathsf{bulk}(r) & r \ge d_\mathsf{l}/2\,, \end{cases}$$

(28)
$$U_\mathsf{bulk}(r) = (U_\mathsf{g} + U_\mathsf{frame}) \tanh\left(\frac{r - d_\mathsf{l}/2}{\alpha}\right)\,,$$

(29)
$$U_\mathsf{lam}(r) = 2U_\mathsf{l}\left(1 - \frac{4r^2}{d_\mathsf{l}^2}\right)\,,$$

with $\alpha = 5 \times 10^{-5}\,\mathrm{m}$. In 2D, the radial coordinate is $r = |y|$, and in 3D $r = \sqrt{y^2 + z^2}$. The frame velocity $U_\mathsf{frame} = -\frac{1}{2}U_\mathsf{g}$ is added to limit the necessary artificial speed of sound and thereby increase the time step size.
The instability is seeded through an initial superimposed sinusoidal velocity perturbation U_y, which in 2D simulations as visualized in the lower half of Fig. 4 is given by

(30)
$$U_\mathsf{y}^\mathsf{2D}(x,r) = \sum_{k=0}^{2} A \sin\left(\frac{2\pi}{\lambda_\mathsf{k}}x\right) \exp\left(-\frac{2\pi}{\lambda_\mathsf{k}}\left|\left(r - \frac{d_\mathsf{l}}{2}\right)\right|\right)\,,$$

with the amplitude $A = 0.01\,U_g$.
In 3D simulations, a dependency on the tangential coordinate φ is added:

(31)
$$U_\mathsf{y}^\mathsf{3D}(x,r,\varphi) = \sum_{k=0}^{2} \sin\left(\frac{2\pi}{\lambda_k}\varphi\right) \cdot \sum_{k=0}^{2} A \sin\left(\frac{2\pi}{\lambda_\mathsf{k}}x\right) \exp\left(-\frac{2\pi}{\lambda_\mathsf{k}}\left|\left(r - \frac{d_\mathsf{l}}{2}\right)\right|\right)\,.$$

The induced wave lengths are λ_k with the smallest wave length $\lambda_0 = L/4$:

(32)
$$\lambda_\mathsf{k} = 2^k \lambda_0\,.$$

5.2. 2D Jet

The fluid distributions resulting from the growing Kelvin-Helmholtz instability in 2D are shown in Fig. 5 for 3 separate instances in time. The baseline MFM computation with $N_1 = 200$ and $h_1 = 1.5dx$ is shown in Fig. 5a. At $t = 0.3\,\mathrm{ms}$, the jet surface exhibits one dominant primary wave and a minor secondary wave. As the instability continues to grow, the dominance of the primary wave is amplified and at $t = 0.6\,\mathrm{ms}$, solitary particles are stripped from its crest. Progressing from this, thin fluid ligaments protruding from the wave crest evolve. At $t = 2.0\,\mathrm{ms}$, these ligaments have been stretched to a point where they have started to disintegrate into solitary particles as well as some larger fragments.
Fig. 5b shows a comparative MFM simulation with $N_2 = 300$. As a consequence of this higher spatial resolution, the growth of the instability is moderately increased with an apparent ligament development evident at $t = 0.6\,\mathrm{ms}$. Subsequently, the fluid distribution continues to evolve qualitatively very similar to the baseline result with the final distribution at $t = 2.0\,\mathrm{ms}$ exhibiting analogous ligaments. However, the disintegration results in a higher number of substantive fluid structures and less solitary particles compared to the baseline. This is an indication of convergence in pri-

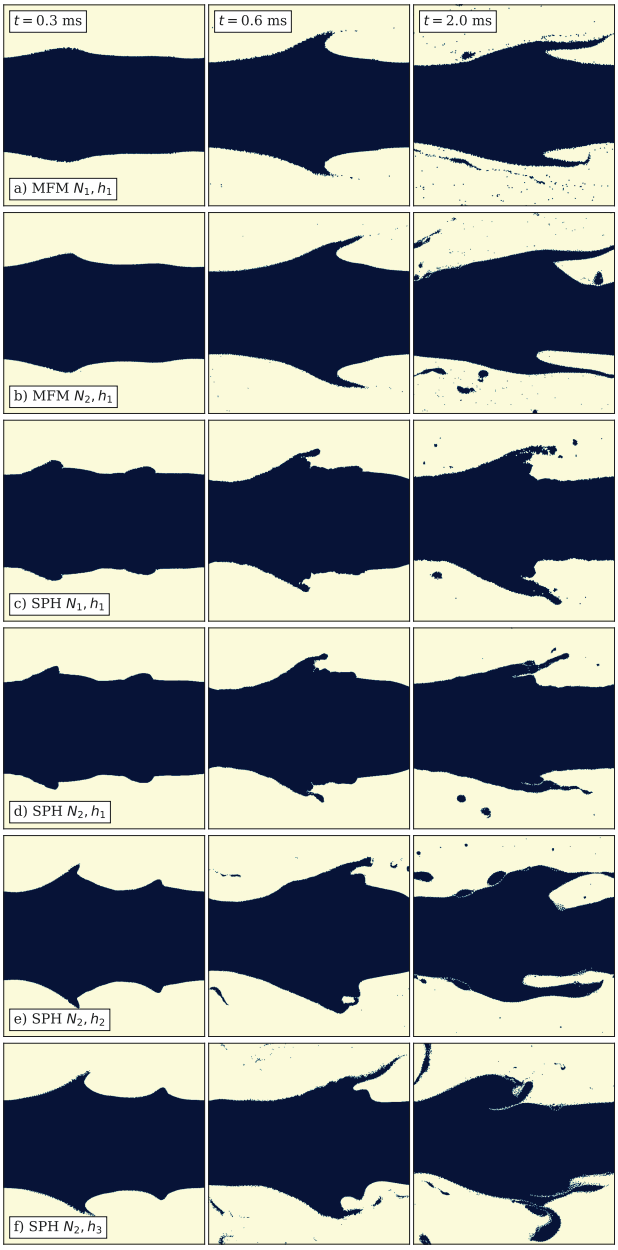

FIG 5. Fluid distribution in the 2D Kelvin-Helmholtz instability benchmark for computations with MFM and SPH using varied number of particles N^2 and smoothing length h at 3 different times t.

mary atomization [28], illustrating MFM's favourable convergence properties independent of the kernel radius.

The results from analogous SPH calculations are displayed in Fig. 5c and 5d. To start, the perturbations on the jet surface appear to be increased but more chaotic, and the secondary wave is more significant. After the initial stages, the evolution of fluid ligaments is impeded, resulting in shorter, more deformed structures compared to MFM. These observed differences are not significantly effected by the increased number of particles from $40,000$ in 5c to $90,000$ in 5d, although the ligaments that do evolve are moderately more delicate in the latter simulation.

As formal convergence in SPH is, contrarily to MFM, dependent on the ratio of smoothing length to particle spacing, two additional computations with the higher number of particles are performed and displayed in Figs. 5e and 5f with $h_2 = 2dx$ and $h_3 = 3dx$, respectively. In both simulations, an accelerated growth of the instability with less chaotic perturbation can be observed at $t = 0.3\,\text{ms}$. For h_3 the fluid distribution at $t = 0.6\,\text{ms}$ is, while still palpably different, more similar to the MFM simulation with N_2. This observation holds true for h_2, though to a lesser extent. The effect of the modified kernel is more pronounced at $t = 2.0\,\text{ms}$. Here, the strongest similarity between MFM and SPH can be observed between Fig. 5b and 5e, even though the ligaments are still less delicate in the SPH results. The distribution in 5f on the other hand bears almost no resemblance to either MFM or SPH results obtained with h_1 or h_2.

In the pursuit of an explanation for the large differences between MFM and SPH results, an investigation into the behaviour of the gas phase is conducive. This is visualized in Fig. 6 through the y-velocity component u_y in the same simulations at the same time steps as in Fig. 5. Again, there is a strong similarity between the two MFM simulations in Fig. 6a and 6b with slightly decreased noise for N_2. In comparison, the two SPH simulations with h_1 in Fig. 6c and 6d are characterized by a substantially higher level of noise, with again only a slight decrease with the higher number of particles. As a result of this noise, more turbulent kinetic energy is dissipated, resulting in a much lower magnitude of u_y at the final time $t = 2\,\text{ms}$ compared to MFM. With increasing smoothing length in the simulations depicted in Fig. 6e and 6f, the noise is decreased and consequently the magnitude of u_y increased.

With this observation, the shorter and less delicate fluid structures in the later stages of the first three SPH simulations can be explained by the higher dissipation of energy and less distinct vortices of the gaseous flow compared to the MFM results. The peculiar behaviour in Fig. 5f might be caused by a decreased effective resolution due to the larger smoothing length h_3. As of now, the increased initial instability growth in SPH compared to MFM, particularly of the secondary instability, remains unexplained. Again this might be caused by the higher level of noise in the SPH simulations. Consequently, the physical validity of the increased growth is questionable.

5.3. 3D Jet

In addition to the 2D simulations, the benchmark is computed in three dimensions using both SPH and MFM with N_1^3 particles and a Wendland C4 kernel with the smoothing length h_1. The resulting deformed liquid jets are displayed in Fig. 7. The different characteristics of MFM and SPH in this benchmark as observed in 2D persist in 3D. Initially, at $t = 0.3\,\text{ms}$, the SPH result exhibit an accelerated and more chaotic growth of the instability. At $t = 0.6\,\text{ms}$, it can be ob-

served that while the jet is still less perturbed for MFM, there is a thin membrane protruding from the crest of the dominant wave. Even though clusters with less than 10 liquid particles are excluded from display to increase visibility, the beginning of the disintegration is evident. In comparison, the fluid structures resulting from SPH are much less delicate.
Subsequently, the level of chaos increases while the general differences between SPH and MFM persist. The MFM result exhibits elongated membranes and ligaments that disintegrate at the edges at $t = 1.0$ ms. In SPH in comparison, the waves continue to grow further in radial direction, while the development of elongated structures parallel to the bulk flow is much

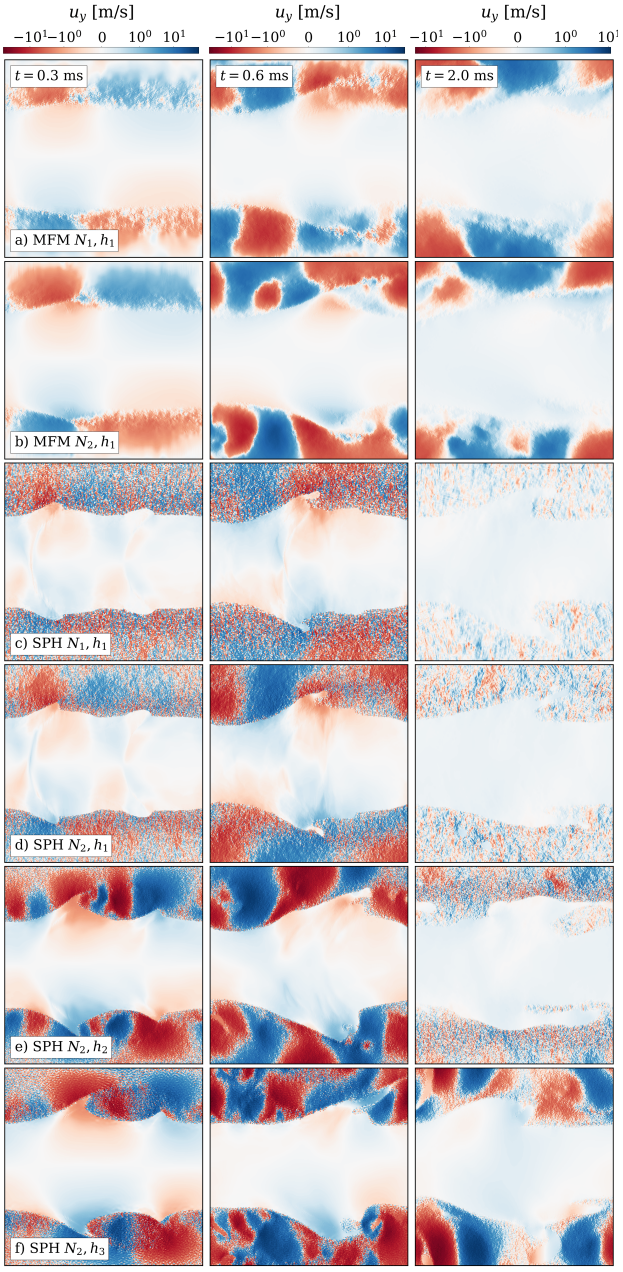

FIG 6. Velocity component in y-direction in the 2D Kelvin-Helmholtz benchmark case for computations with MFM and SPH using varied number of particles N^2 and smoothing length h at 3 different times t.

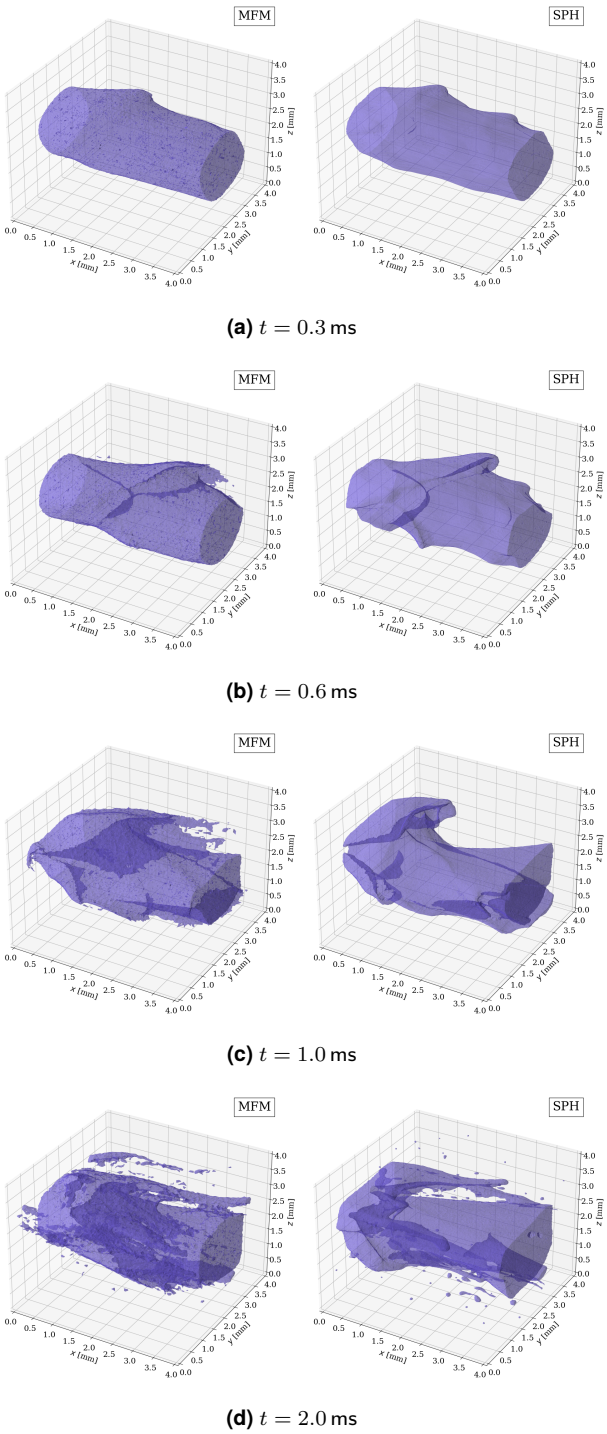

(a) $t = 0.3$ ms

(b) $t = 0.6$ ms

(c) $t = 1.0$ ms

(d) $t = 2.0$ ms

FIG 7. 3D liquid jet computed using MFM and SPH with N_1^3 particles and smoothing length h_1.

less pronounced. At the end of the simulation at $t = 2.0$ ms, both cases show a substantial number of larger droplets stripped off from the bulk jet. In MFM, these droplets are results of the disintegration of ligaments which in turn are formed from membranes. In the case of the SPH simulation, fewer droplets are formed from shorter ligaments and the development of membranes is almost non-existent. Overall, these 3D simulations confirm the observations made in 2D.

6. CONCLUSION

In this work, a surface tension model was integrated and validated in a Meshless-Finite-Mass code. It was demonstrated that through the inclusion of SPH models, MFM might be a viable alternative for the numerical analysis of engineering applications. Furthermore, this facilitated a first-time comparison of MFM and SPH in technically relevant multi-phase flows.

For further analysis, a Kelvin-Helmholtz configuration resembling primary atomization was proposed. The difference in the behaviour of the two methods in this benchmark case is apparent. The MFM results exhibit an enhanced evolution of long, thin fluid structures and reduced small scale noise in the velocity field. While MFM reacts predictably and favourably to an increase of the number of particles, the assessment of the spatial resolution of the SPH simulations is ambiguous. A conclusive evaluation of which combination of particle number and kernel size performed best is not possible.

Even though these differences are evident, their classification is troublesome. Due to the simplified nature of the setup with its periodic boundaries, the instability growth deviates significantly from the behaviour established in literature [3, 27]. Therefore, a critical examination of the applicability to realistic problems is necessary. First, the observations of the early stages of the instability growth cannot simply be transferred to more complex multi-phase problems, in which instabilities are not artificially seeded but rather induced through chaotic perturbation of the interface. Second, while MFM leads to an enhanced development of very delicate fluid structures, the significance to reality is uncertain. It is to be expected, that membranes as they can be seen on the left hand side in Figs. 7c and 7d would disintegrate at a much earlier state compared to the structures present in the SPH result.

Even considering these uncertainties, this work clearly shows that in multi-phase applications where SPH is used due to its inherent ability to capture complex interface deformation, MFM has the potential to improve accuracy of numerical analysis if turbulence is a factor.

Contact address:

markus.wicker@kit.edu

References

[1] Samuel Braun, Lars Wieth, Simon Holz, Thilo F. Dauch, Marc C. Keller, Geoffroy Chaussonnet, Sebastian Gepperth, Rainer Koch, and Hans-Jörg Bauer. Numerical prediction of air-assisted primary atomization using smoothed particle hydrodynamics. *International Journal of Multiphase Flow*, 114:303–315, 2019. ISSN: 03019322. DOI: 10.1016/j.ijmultiphaseflow.2019.03.008.

[2] Rainer Koch, Samuel Braun, Lars Wieth, Geoffroy Chaussonnet, Thilo Dauch, and Hans-Jörg Bauer. Prediction of primary atomization using smoothed particle hydrodynamics. *European Journal of Mechanics - B/Fluids*, 61:271–278, 2017. ISSN: 09977546. DOI: 10.1016/j.euromechflu.2016.10.007.

[3] G. Chaussonnet, S. Braun, T. Dauch, M. Keller, A. Sänger, T. Jakobs, R. Koch, T. Kolb, and H.-J. Bauer. Toward the development of a virtual spray test-rig using the smoothed particle hydrodynamics method. *Computers & Fluids*, 180:68–81, 2019. ISSN: 00457930. DOI: 10.1016/j.compfluid.2019.01.010.

[4] T. F. Dauch, G. Chaussonnet, M. C. Keller, M. Okraschevski, C. Ates, R. Koch, and H.-J. Bauer. 3d predictions of the primary breakup of fuel in spray nozzles for aero engines. In Wolfgang E. Nagel, Dietmar H. Kröner, and Michael M. Resch, editors, *High Performance Computing in Science and Engineering '20*, pages 419–433. Springer International Publishing, Cham, 2021. ISBN: 978-3-030-80601-9. DOI: 10.1007/978-3-030-80602-6_27.

[5] R. A. Gingold and J. J. Monaghan. Smoothed particle hydrodynamics: theory and application to non-spherical stars. *Monthly Notices of the Royal Astronomical Society*, 181(3):375–389, 1977. ISSN: 0035-8711. DOI: 10.1093/mnras/181.3.375.

[6] Leon B. Lucy. A numerical approach to the testing of the fission hypothesis. *Astronomical Journal, vol. 82, Dec. 1977, p. 1013-1024.*, 82:1013–1024, 1977.

[7] J. J. Monaghan. Simulating free surface flows with sph. *Journal of Computational Physics*, 110(2):399–406, 1994. ISSN: 00219991. DOI: 10.1006/jcph.1994.1034.

[8] Andreas Bauer and Volker Springel. Subsonic turbulence in smoothed particle hydrodynamics and moving-mesh simulations. *Monthly Notices of the Royal Astronomical Society*, 423(3):2558–2578, 2012. ISSN: 0035-8711. DOI: 10.1111/j.1365-2966.2012.21058.x.

[9] Philip F. Hopkins. A new class of accurate, mesh-free hydrodynamic simulation methods. *Monthly Notices of the Royal Astronomical Society*, 450(1):53–110, 2015. ISSN: 0035-8711. DOI: 10.1093/mnras/stv195.

[10] S. Adami, X. Y. Hu, and N. A. Adams. A new surface-tension formulation for multi-phase sph using a reproducing divergence approximation. *Journal of Computational Physics*, 229(13):5011–5021, 2010. ISSN: 00219991. DOI: 10.1016/j.jcp.2010.03.022.

[11] D. Lecoanet, M. McCourt, E. Quataert, K. J. Burns, G. M. Vasil, J. S. Oishi, B. P. Brown,

J. M. Stone, and R. M. O'Leary. A validated nonlinear kelvin–helmholtz benchmark for numerical hydrodynamics. *Monthly Notices of the Royal Astronomical Society*, 455(4):4274–4288, 2016. ISSN: 0035-8711. DOI: 10.1093/mnras/stv2564.

[12] Colin P. McNally, Wladimir Lyra, and Jean-Claude Passy. A well-posed kelvin-helmholtz instability test and comparison. *The Astrophysical Journal Supplement Series*, 201(2):18, 2012. ISSN: 0067-0049. DOI: 10.1088/0067-0049/201/2/18.

[13] Terrence S. Tricco. The kelvin–helmholtz instability and smoothed particle hydrodynamics. *Monthly Notices of the Royal Astronomical Society*, 488(4):5210–5224, 2019. ISSN: 0035-8711. DOI: 10.1093/mnras/stz2042.

[14] Daniel J. Price. Smoothed particle hydrodynamics and magnetohydrodynamics. *Journal of Computational Physics*, 231(3):759–794, 2012. ISSN: 00219991. DOI: 10.1016/j.jcp.2010.12.011.

[15] X. Y. Hu and N. A. Adams. A multi-phase sph method for macroscopic and mesoscopic flows. *Journal of Computational Physics*, 213(2):844–861, 2006. ISSN: 00219991. DOI: 10.1016/j.jcp.2005.09.001.

[16] K. Szewc, J. Pozorski, and J.-P. Minier. Analysis of the incompressibility constraint in the smoothed particle hydrodynamics method. *International Journal for Numerical Methods in Engineering*, 92(4):343–369, 2012. ISSN: 00295981. DOI: 10.1002/nme.4339.

[17] Robert H. Cole and Royal Weller. Underwater explosions. *Physics Today*, 1(6):35, 1948. ISSN: 0031-9228. DOI: 10.1063/1.3066176.

[18] Philip F. Hopkins. Anisotropic diffusion in meshfree numerical magnetohydrodynamics. *Monthly Notices of the Royal Astronomical Society*, 466(3):3387–3405, 2017. ISSN: 0035-8711. DOI: 10.1093/mnras/stw3306.

[19] Nathalie Lanson and Jean-Paul Vila. Renormalized meshfree schemes ii: Convergence for scalar conservation laws. *SIAM Journal on Numerical Analysis*, 46(4):1935–1964, 2008. ISSN: 0036-1429. DOI: 10.1137/S003614290444739X.

[20] Nathalie Lanson and Jean-Paul Vila. Renormalized meshfree schemes i: Consistency, stability, and hybrid methods for conservation laws. *SIAM Journal on Numerical Analysis*, 46(4):1912–1934, 2008. ISSN: 0036-1429. DOI: 10.1137/S0036142903427718.

[21] Volker Springel. The cosmological simulation code gadget-2. *Monthly Notices of the Royal Astronomical Society*, 364(4):1105–1134, 2005. ISSN: 0035-8711. DOI: 10.1111/j.1365-2966.2005.09655.x.

[22] E. F. Toro. The hllc riemann solver. *Shock Waves*, 29(8):1065–1082, 2019. ISSN: 0938-1287. DOI: 10.1007/s00193-019-00912-4.

[23] S. Nugent and H. A. Posch. Liquid drops and surface tension with smoothed particle applied mechanics. *Physical Review E*, 62(4):4968–4975, 2000. ISSN: 1063-651X. DOI: 10.1103/PhysRevE.62.4968.

[24] J.U Brackbill, D.B Kothe, and C. Zemach. A continuum method for modeling surface tension. *Journal of Computational Physics*, 100(2):335–354, 1992. ISSN: 00219991. DOI: 10.1016/0021-9991(92)90240-Y.

[25] Holger Wendland. Piecewise polynomial, positive definite and compactly supported radial functions of minimal degree. *Advances in Computational Mathematics*, 4(1):389–396, 1995. ISSN: 1019-7168. DOI: 10.1007/BF02123482.

[26] Walter Dehnen and Hossam Aly. Improving convergence in smoothed particle hydrodynamics simulations without pairing instability. *Monthly Notices of the Royal Astronomical Society*, 425(2):1068–1082, 2012. ISSN: 0035-8711. DOI: 10.1111/j.1365-2966.2012.21439.x.

[27] A. Sänger, T. Jakobs, N. Djordjevic, and T. Kolb. Effect of primary instability of a high viscous liquid jet on the spray quality generated by a twin-fluid atomizer. In Lydia Achelis, editor, *26th European Conference Liquid Atomization and Spray Systems*. Bremen, 2014. ISBN: 978-3-00-047070-7.

[28] Samuel Braun, Simon Holz, L. Wieth, Thilo F. Dauch, Marc C. Keller, Geoffroy Chaussonnet, Corina Schwitzke, and Hans-Jörg Bauer. Hpc predictions of primary atomization with sph : Validation and comparison to experimental results. In *12th International SPHERIC Workshop, Ourense, E, J*, 2017. DOI: 10.5445/IR/1000070593.